

RESEARCH ARTICLE | FEBRUARY 15 2024

# Low-threshold single ternary GaAsSb nanowire lasers emitting at silicon transparent wavelengths

P. Schmiedeke ; C. Doganlar ; H. W. Jeong ; M. Döblinger ; J. J. Finley ; G. Koblmüller  *Appl. Phys. Lett.* 124, 071112 (2024)<https://doi.org/10.1063/5.0191070>

CrossMark

**A total solution for low-temperature characterization**[Learn more >](#)

# Low-threshold single ternary GaAsSb nanowire lasers emitting at silicon transparent wavelengths

Cite as: Appl. Phys. Lett. **124**, 071112 (2024); doi: [10.1063/5.0191070](https://doi.org/10.1063/5.0191070)

Submitted: 11 December 2023 · Accepted: 31 January 2024 ·

Published Online: 15 February 2024



View Online



Export Citation



CrossMark

P. Schmiedeke,<sup>1</sup> , C. Doganlar,<sup>1</sup> , H. W. Jeong,<sup>1</sup> , M. Döblinger,<sup>2</sup> , J. J. Finley,<sup>1</sup> and G. Koblmüller<sup>1,a)</sup>

## AFFILIATIONS

<sup>1</sup>Walter Schottky Institute and Physics Department, School of Natural Sciences, Technical University of Munich, Garching, Germany

<sup>2</sup>Department of Chemistry, Ludwig-Maximilians-University Munich, Munich, Germany

<sup>a)</sup>Author to whom correspondence should be addressed: [Gregor.KoblmueLLer@wsi.tum.de](mailto:Gregor.KoblmueLLer@wsi.tum.de)

## ABSTRACT

Conventional binary III–V nanowire (NW) lasers face substantial challenges in tuning their lasing emission to silicon transparent wavelengths and require complex quantum heterostructure designs for realizing on-chip integrated nanolasers. Here, an alternative and straightforward approach is reported by developing ternary III–V NW-lasers in the form of surface-passivated GaAsSb NW-lasers grown on silicon. High-quality GaAsSb NW-cavities with high Sb-content ( $>20\%$ ) and extended lengths ( $>5\ \mu\text{m}$ ) are shown to exhibit striking radiative efficiency enhancements ( $\sim 200$ -fold) when passivated by closely lattice-matched InAlGaAs shell layers. Utilizing this core-shell approach, optically pumped lasing is then demonstrated from single GaAsSb NW-lasers with lasing threshold as low as  $3.2\ \mu\text{J}/\text{cm}^2$  at temperatures up to 250 K and emission wavelengths of  $\sim 1.1$ – $1.2\ \mu\text{m}$ . Analysis of the optical mode spectra and mode-dependent threshold gain further shows that lasing is induced by the fundamental HE<sub>11</sub> modes, and likely even lower thresholds may be achieved by establishing the TE<sub>01</sub> mode at increased NW-cavity diameters.

© 2024 Author(s). All article content, except where otherwise noted, is licensed under a Creative Commons Attribution (CC BY) license (<http://creativecommons.org/licenses/by/4.0/>). <https://doi.org/10.1063/5.0191070>

The recent demonstrations of lasing action from III–V semiconductor nanowire (NW) lasers integrated on silicon (Si)<sup>1,2</sup> and silicon-on-insulator (SOI) photonic waveguides and circuits<sup>3–6</sup> have highlighted their great application potentials as ultracompact on-chip coherent light sources in Si-photonics and high-speed optical communication systems.<sup>7</sup> Together with their high  $\beta$ -factors<sup>1</sup> and ultrafast dynamics,<sup>1,6,8</sup> a key advantage of NW-lasers is, hereby, their site-selective integration and straightforward coupling scheme of their emission into Si-waveguides, as shown in epitaxial, vertical-cavity NW-lasers,<sup>3,9</sup> 1D-nanobeam-cavity lasers,<sup>4</sup> and NW-lasers integrated into Si-slot waveguides of 2D-photonic crystal (PhC) cavities.<sup>6</sup> Naturally, this requires active gain media in NW-lasers that emit at Si-transparent wavelengths ( $>1.1\ \mu\text{m}$ ) to minimize absorption losses of coupled lasing emission propagating in the underlying Si-photonics circuit.

Most of the III–V NW-lasers investigated to date are based on either the InP<sup>10,11</sup> or GaAs-NW<sup>1,4,12–14</sup> platform. Given their unsuitable bandgap energies [1.42 eV (GaAs) and 1.34 eV (InP)], access to Si-transparent wavelengths has been made possible only by the incorporation of other active gain media, typically in the form of stacks of coaxial multi-quantum wells (MQWs)<sup>2,15,16</sup> or axial multi-quantum disks/dots (MQDs).<sup>5,6,17</sup> However, in such structures—especially those

built from the GaAs NW-platform—the cumulative strain in the stacks has limited the emission wavelengths mostly to  $\sim 0.8$ – $1\ \mu\text{m}$ .<sup>18–21</sup>

To mitigate this, band-engineered ternary III–V NWs are reckoned a more versatile platform, as they may serve, already in their bulk form, as lasing medium itself (if the bandgap can be engineered toward the Si-transparency window) or provide a strain-reduced virtual substrate for core-shell MQW and MQD NW-lasers. Indeed, bandgap tunable InGaAs and InAsP NW-lasers have been reported<sup>4,22,23</sup> but because of their growth limited dimensions they could only exhibit lasing action when placed into external PhC-array cavities. Hence, true ternary III–V NW-lasers that take advantage of their own intrinsic resonator cavity are still missing.

In this Letter, we report mixed III–V–V ternary GaAsSb NW-lasers with bandgap tailored to energies below the Si bandgap to realize optically pumped lasing at Si-transparent wavelengths ( $\sim 1.1$ – $1.2\ \mu\text{m}$ ) with low threshold and operation close to room-temperature. This achievement is based on the formation of high-quality GaAsSb NWs with extended cavity lengths directly on Si, and the use of lattice-matched InAlGaAs surface passivation to dramatically enhance the radiative efficiency. The GaAsSb NW-lasers are grown by selective-area molecular beam epitaxy (MBE) on prepatterned SiO<sub>2</sub>/Si(111)

substrates, adapting recently established self-catalyzed vapor-liquid-solid (VLS) growth schemes for high-quality, phase-pure NWs with uniform, non-tapered resonator geometry.<sup>24</sup>

Two sets of NW samples are presented, both containing an additional quaternary InAlGaAs shell passivation, and which aim to demonstrate (i) the effect of the InAlGaAs shell, with varying shell composition, on the optical emission enhancement, and (ii) its application to realize GaAsSb-NW lasers with cavity dimensions tailored toward high mode confinement. The first set consists of GaAsSb NWs grown at 660 °C for 60 min at a fixed Ga-flux of 0.6 Å/s, As-BEP (beam equivalent pressure) of  $4 \times 10^{-6}$  mbar, and Sb-BEP of  $7.7 \times 10^{-7}$  mbar, employing a GaAs NW-nucleation stem (15 min of growth), as in our previous work.<sup>24</sup> The GaAsSb NW cores, with an expected Sb-content of ~20%, are then overgrown by a quaternary InAlGaAs shell with a thickness of ~18 nm (at 420 °C, As-BEP of  $4 \times 10^{-5}$  mbar). Three different shell compositions close to lattice-matching are studied; i.e., nominally  $\text{In}_{0.21}\text{Al}_{0.34}\text{Ga}_{0.45}\text{As}$ ,  $\text{In}_{0.28}\text{Al}_{0.36}\text{Ga}_{0.36}\text{As}$ , and  $\text{In}_{0.38}\text{Al}_{0.31}\text{Ga}_{0.31}\text{As}$  (for simplicity also referred to as 21%-In, 28%-In, and 38%-In later on).

Figure 1 shows typical scanning electron microscopy (SEM) images of the GaAsSb-InAlGaAs core-shell NWs, illustrating perfectly site-controlled growth with very high uniformity in length [Fig. 1(a)] and diameter [Fig. 1(b)]. The NWs have a total length of ~6.6 μm, whereby the bottom part (~1.8 μm) consists of the GaAs stem in this case. The GaAsSb core diameter is about 170 nm wide, illustrated by the image of a reference (core-only) NW in Fig. 1(c). The core-shell NW has a total diameter of ~210 nm [Fig. 1(d)], suggesting an InAlGaAs shell thickness close to the nominal value of ~20 nm.

The core-shell structure is verified by high-resolution scanning transmission electron microscopy (HR-STEM) and EDXS (energy-dispersive x-ray spectroscopy) analysis performed in a 300 kV-FEI Titan Themis TEM on specimen prepared by focused ion beam. Figure 1(e) shows a high-angle annular dark field (HAADF) STEM image of the cross section of a GaAsSb-InAlGaAs core-shell NW, grown with the highest In-content, i.e.,  $\text{In}_{0.38}\text{Al}_{0.31}\text{Ga}_{0.31}\text{As}$ . From the atomic number (Z) contrast, the InAlGaAs shell is approximately  $20 \pm 2$  nm thick, as expected, while the GaAsSb core appears to be composed of two regions, i.e., an inner core with a bright contrast (indicative of high Sb-content) and a surrounding GaAsSb shell with slightly less Sb-content given the reduced contrast. This GaAsSb NW structure is confirmed by EDXS mapping (see the supplementary material), resulting in an Sb-content of ~20% in the inner core and ~15% in the adjacent shell (5% accuracy of EDXS analysis). These compositions of the inner core and the GaAsSb shell are uniform along the NW growth axis, as confirmed in our recent study.<sup>24</sup> As explained in Ref. 24, the center (Sb-rich) region is attributed to the VLS-GaAsSb growth along the NW-axis, whereas the surrounding region stems from a spontaneous vapor-solid (VS) sidewall growth that stabilizes the non-tapered NW-morphology via step-flow growth.<sup>24</sup> EDXS analysis of the InAlGaAs shell yields an In-content of  $\sim 36 \pm 5\%$ , and Al- and Ga-content of  $\sim 27 \pm 5\%$  and  $\sim 37 \pm 5\%$  (see the supplementary material), which agrees with the nominal values within the experimental error of EDXS.

To demonstrate the effect of the InAlGaAs shell passivation on the radiative efficiency, micro-photoluminescence ( $\mu$ -PL) spectroscopy is performed on single NWs at 10 K in a He-flow cryostat. Hereby, individual NWs are excited in their standing geometry (on Si substrate) using a mode-locked titanium-sapphire laser (1.59 eV excitation

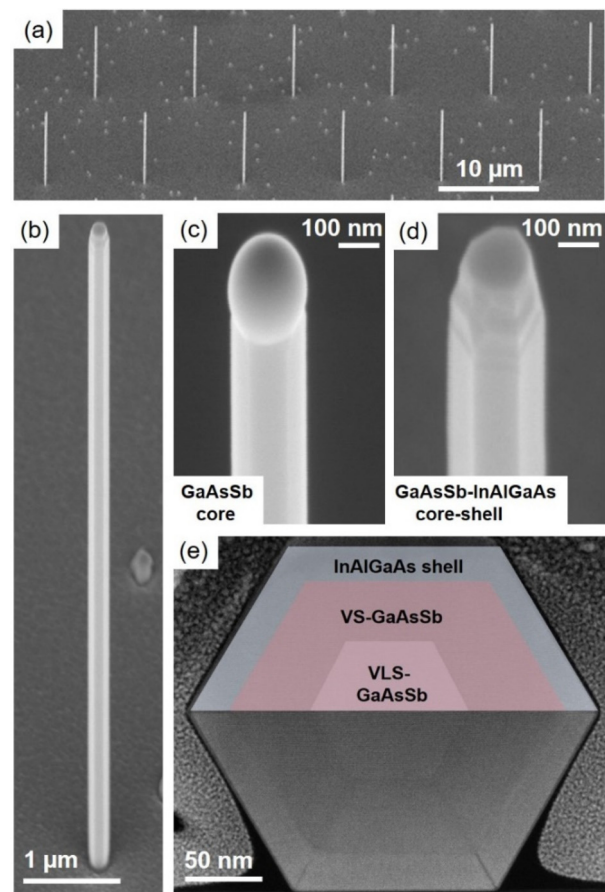


**FIG. 1.** SEM images of InAlGaAs-passivated GaAsSb NWs, showing (a) overview image of a NW-array with pitch of 10 μm; (b) higher magnification of a single NW; (c) core-only GaAsSb reference showing the Ga-droplet at the NW-tip; and (d) corresponding image of the core-shell GaAsSb-InAlGaAs NW. (e) Cross-sectional STEM-HAADF image and overlaid, color-coded schematic of the GaAsSb-InAlGaAs core-shell structure, depicting the different regions from the GaAsSb core and the outer InAlGaAs shell layer.

energy, 200-fs pulse length, and 82 MHz repetition rate) confined to a spot size of  $\sim 2$  μm. The emission from the NW is collected using an  $\text{LN}_2$ -cooled InGaAs CCD camera. Figure 2 compares the PL data for the InAlGaAs-passivated NWs and the unpassivated core-only NW reference, probed under varying excitation pump fluences. For the unpassivated GaAsSb NW, two emission peaks are observed at lowest pump fluence, i.e., at 1.10 and 1.16 eV. In line with Ref. 24, the peak at low energy stems from the Sb-rich VLS-GaAsSb NW-core, while the peak at higher energy is related to the spontaneous VS-GaAsSb layer that has slightly less Sb-content [cf. Fig. 1(e)]. The double-peak structure is, however, not observed on all NWs of this sample. Especially, at very low pump fluence, most NWs show a single emission peak at 1.09 eV (see the supplementary material), reflecting the lowest bandgap of the native GaAsSb core. Nevertheless, with increasing pump fluence, both the low and high energy peaks develop into one broader peak that rises weakly in intensity with pump fluence.

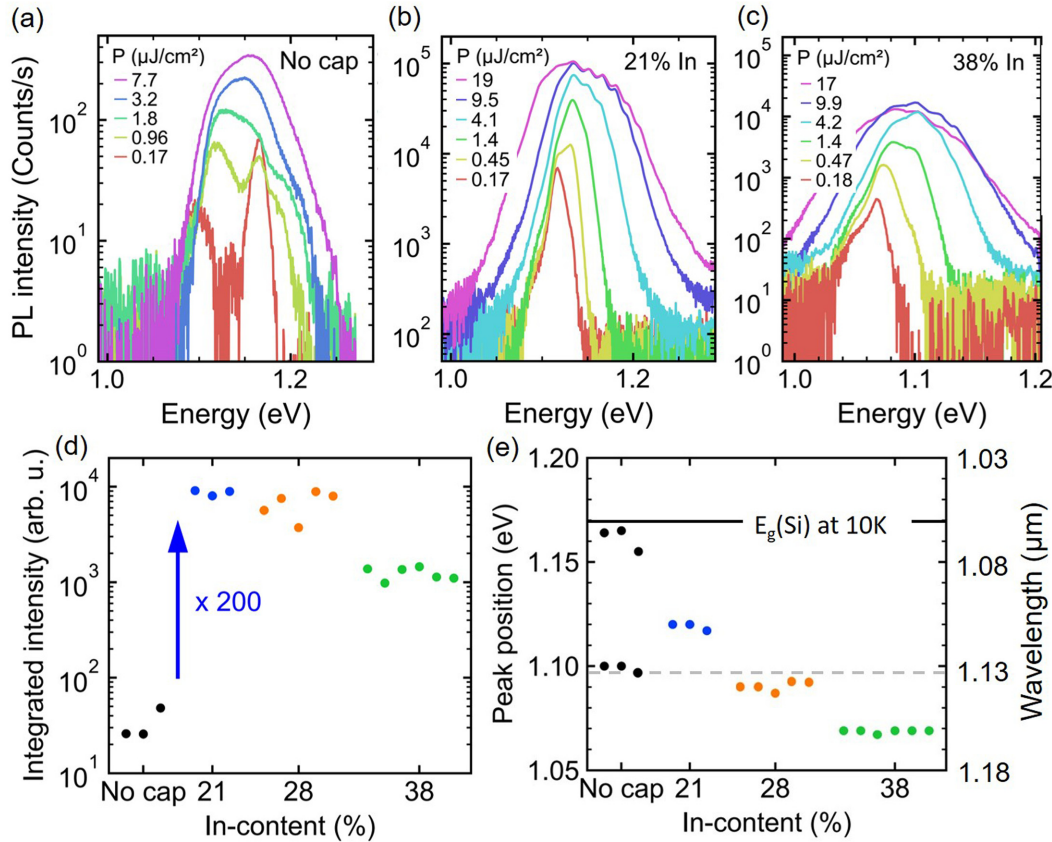


**FIG. 2.** Pump-fluence dependent PL spectra of single GaAsSb NWs at 10 K, for (a) unpassivated (core-only) NW, and passivated NWs with two different shell compositions: (b)  $\text{In}_{0.21}\text{Al}_{0.34}\text{Ga}_{0.45}\text{As}$  and (c)  $\text{In}_{0.38}\text{Al}_{0.31}\text{Ga}_{0.31}\text{As}$ . (d) Maximum integrated PL intensity of all samples with different shell In-contents, compared to the unpassivated NW. Datapoints for each color correspond to the number of NWs probed from each sample (black—core-only, blue—21%-In, orange—28%-In, and green—38%-In), which are offset along the x-axis for clarity; (e) corresponding PL peak energies at lowest pump fluence ( $0.17 \mu\text{J}/\text{cm}^2$ ). The dashed line at 1.10 eV indicates the native GaAsSb NW core reference, and the solid line at 1.17 eV marks the Si bandgap energy at 10 K.

The spectra of Figs. 2(b) and 2(c), shown for NWs with two different InAlGaAs shell compositions (i.e.,  $\text{In}_{0.21}\text{Al}_{0.34}\text{Ga}_{0.45}\text{As}$  and  $\text{In}_{0.38}\text{Al}_{0.31}\text{Ga}_{0.31}\text{As}$ , as well as a third intermediate composition,  $\text{In}_{0.28}\text{Al}_{0.36}\text{Ga}_{0.36}\text{As}$ , see the supplementary material), evidence some markedly different behavior compared to the unpassivated NWs. First, the intensity rises more rapidly in all passivated NWs, reaching much higher peak intensity, while broadening more significantly with pump fluence, compared to the unpassivated NW. Particularly, broadening is found on both the high- and low-energy sides of the peak emission, reflecting the increased band-filling and bandgap renormalization, respectively, as the carrier density is increased. At very high pump fluence, the spectra are weakly modulated by equally spaced peaks on the high-energy side, which are likely due to Fabry-Pérot (FP) resonances. In contrast, the absence of significant broadening and the rather early saturation in PL intensity of the unpassivated NWs indicate increased non-radiative carrier recombination. Indeed, plots of the integrated intensity vs pump fluence (see the supplementary material) confirm saturation and even declining PL intensity (due to onset of lattice heating), while at equivalent power density, such behavior is not observed for the passivated NWs.

The most striking evidence for the superior radiative efficiency of the passivated NWs is seen by comparing the maximum integrated intensity of all NW-samples [Fig. 2(d)]. Here, each datapoint (color) refers to an individual NW recorded from each sample ( $\sim 3$ – $6$  NWs/sample). The data show that, while the integrated intensity varies only marginally between NWs from a given sample, the difference in intensity between the passivated and unpassivated NWs is striking. For example, for passivated NWs with In-content of 21% and 28% the integrated intensity is  $\sim 200$  times higher compared to the core-only GaAsSb NWs. Similar increases by more than 2 orders of magnitude are also seen when comparing the integrated intensity at fixed pump fluence ( $5 \mu\text{J}/\text{cm}^2$ , see the supplementary material). For the highest In-content of 38%, the PL enhancement is slightly lower, but still about 40-fold enhanced compared to unpassivated NWs. The reason for the lower PL enhancement in this sample is not clear, but could be related to an increased strain compared to the other two passivated NW-samples (21%-In and 28%-In), which are closer to lattice matching with the GaAsSb core region.

In fact, any slight lattice mismatch is expected to also manifest itself as a strain on the GaAsSb core, which shifts its emission energy,



as illustrated in Fig. 2(e) for lowest pump fluence ( $0.17 \mu\text{J}/\text{cm}^2$ ). For the GaAsSb NW-core, we consider here the peak emission at  $1.10 \text{ eV}$  as the native reference energy, in line with the observations in Ref. 24 and the fact that this emission is prominent in all unpassivated NWs at low power. The passivated NW samples with low In-content (21%-In and 28%-In) do not differ much from this peak energy (shifts  $< 20 \text{ meV}$ ), suggesting close lattice-matching conditions. For increased In-content (38%), the emission shows a more pronounced shift,  $\sim 30\text{--}35 \text{ meV}$  to lower energy ( $1.07 \text{ eV}$ , i.e.,  $1.16 \mu\text{m}$ ), suggesting an increased tensile strain in the GaAsSb core. Yet, the strain is considerably low, as such small peak-shifts are within typical values for closely lattice-matched III-V core-shell NWs,<sup>25,26</sup> compared to highly mismatched NW-systems where peak shifts are  $> 100 \text{ meV}$ .<sup>16,27,28</sup>

Ultimately, NW-lasers are realized by exploiting the beneficial InAlGaAs-passivation approach. Hereby, GaAsSb NWs are grown under nearly identical conditions as those above, but with slightly higher Ga- ( $0.9 \text{ \AA/s}$ ) and Sb-flux (Sb-BEP of  $1.6 \times 10^{-6} \text{ mbar}$ ), and a nucleating GaAs stem reduced to  $\sim 0.3 \mu\text{m}$ . Under these conditions, the diameter of the NW is increased to  $\sim 260\text{--}270 \text{ nm}$ , while the Sb-content is also slightly increased (i.e.,  $\sim 25\%$ —VLS-GaAsSb core,  $\sim 20\%$ —VS-GaAsSb),<sup>24</sup> in an attempt to shift the emission to longer wavelengths ( $> 1.2 \mu\text{m}$ ). Using a passivating shell with  $\sim 30 \text{ nm}$   $\text{In}_{0.50}\text{Al}_{0.17}\text{Ga}_{0.33}\text{As}$ , the total NW-diameter results in  $\sim 320 \text{ nm}$  and NW-cavity length of  $\sim 5.2 \mu\text{m}$  [Fig. 3(a)].

Figure 3(b) shows spectra of a single NW-laser measured in a lying geometry on a sapphire substrate, confirming the anticipated shift toward longer wavelength. Notably, at lowest pump fluence, the spectrum is characterized by a single peak at  $0.97 \text{ eV}$ , i.e., emission wavelength of  $1.28 \mu\text{m}$  (close to the telecom O-band). With increasing pump fluence, we observe a strong peak broadening to the high energy side and the appearance of distinct FP modes. To characterize lasing behavior, depicted in Fig. 3(c), neutral-density filters are employed to limit the very intense PL signal from saturating signal detection when probed under higher pump fluences. By exciting the NW-laser, first shown here at  $10 \text{ K}$ , sharp peaks appear at  $1.11$ ,  $1.14$ , and  $1.17 \text{ eV}$  for fluences greater than  $\sim 11 \mu\text{J}/\text{cm}^2$ . These peaks rise nonlinearly in intensity reflecting the characteristic transition from amplified spontaneous emission to lasing. Similar observations are also made at higher temperature of  $250 \text{ K}$  [Fig. 3(c), bottom panel], where the transition to stimulated emission occurs naturally at larger pump fluences due to the reduction in peak gain with temperature. Both the spontaneous emission and the lasing peaks (at  $1.06$ ,  $1.09$ , and  $1.12 \text{ eV}$ ) are redshifted by  $\sim 50 \text{ meV}$  compared to data at  $10 \text{ K}$ , indicating thermal bandgap narrowing.

Closer inspection of the spectra at  $10 \text{ K}$  [Figs. 3(b) and 3(c)] suggests a relatively large band-filling that is necessary to reach lasing—i.e., the energy difference between the spontaneous emission at lowest pump fluence ( $0.97 \text{ eV}$ ) and the first lasing peak energy ( $1.11 \text{ eV}$ ) is as high as  $\sim 140 \text{ meV}$ . Such large shift is commonly not seen in other bulk (e.g., GaAs or InP) NW-lasers.<sup>11–13</sup> We attribute the observed shift to the characteristic alloy compositional structure of the GaAsSb NW-core, which is composed of two slightly different Sb-contents (i.e., bandgap energies) in the coaxial direction [cf. Fig. 1(e)]. Thereby, under lowest pump fluences, emission stems from the lowest bandgap [in line with Fig. 2(a)], while at high pump fluences, where lasing occurs, the emission is most likely also from the higher bandgap region of the GaAsSb core.

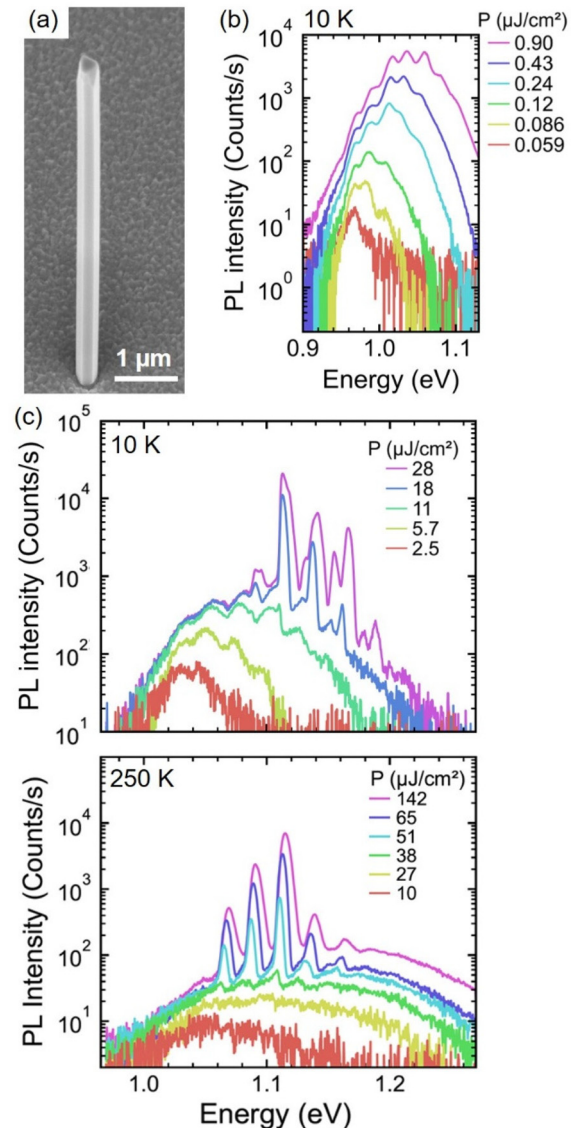


**FIG. 3.** (a) SEM image of an InAlGaAs-passivated GaAsSb NW-laser with length of  $5.2 \mu\text{m}$  and diameter of  $320 \text{ nm}$ ; (b) PL spectra of a NW-laser dispersed on sapphire, and recorded at  $10 \text{ K}$  under low pump fluences; and (c) and (d) semi-logarithmic plots of PL spectra under higher pump fluences at  $10 \text{ K}$  (c) and  $250 \text{ K}$  (d), evidencing distinct lasing peaks at energies between  $\sim 1.06$  and  $1.15 \text{ eV}$ .

To evaluate the lasing thresholds, Fig. 4 presents the input–output (L–L) curves obtained from integrating the PL intensity of all spectra of Fig. 3 over the entire energy range. As shown by the log–log plot [Fig. 4(a)], clear S-shape characteristics are observed for both data at  $10 \text{ K}$  and  $250 \text{ K}$ , indicative of lasing behavior. This is further reflected in the linear representation [Fig. 4(b)], where above threshold the initially weak emission intensity rises by a sudden linear increase with pump fluence. By fitting the linear portion of the L–L curves, the respective lasing thresholds are determined as  $12.1 \mu\text{J}/\text{cm}^2$  ( $10 \text{ K}$ ) and  $45.2 \mu\text{J}/\text{cm}^2$  ( $250 \text{ K}$ ). Other NW-lasers from the same sample were also

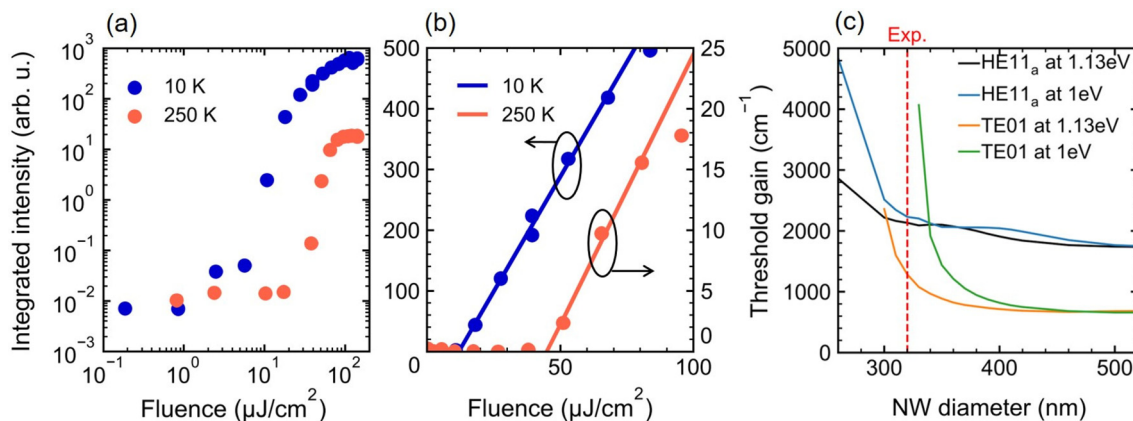


**FIG. 4.** L-L curves in logarithmic (a) and linear (b) representation, illustrating the lasing thresholds of  $12.1 \mu\text{J}/\text{cm}^2$  (10 K) and  $45.2 \mu\text{J}/\text{cm}^2$  (250 K), obtained from linear fits of the integrated intensity; (c) calculated threshold gain as a function of NW diameter at 1 and 1.13 eV for the TE01 and fundamental HE11 modes; the experimentally investigated diameter is marked in red.

investigated at 10 K, with lowest lasing threshold value of  $3.2 \mu\text{J}/\text{cm}^2$  (see the supplementary material).

To bring the lasing characteristics in relation with the underlying transverse optical mode in the NW-cavity, a closer spectral analysis finds that all spectra recorded at 10 K [Fig. 3(c) and supplementary material] exhibit a distinct mode splitting of the lasing peaks that is most pronounced at higher pump fluences. This indicates that the mode structure is not composed of a single transverse mode, but obviously by a set of two split-modes which we ascribe to the fundamental HE11 modes, according to the following observations: First, the energetic spacing of the FP modes at low pump fluence ( $\Delta E \sim 22\text{--}25 \text{ meV}$ ) corresponds to a group refractive index of  $n_g \sim 5.5$  for the given NW-cavity length, which is in line with recent data reported for fundamental HE11 modes in III-V NW-lasers.<sup>13,29</sup> As the FP modes split into pairs upon increased pump fluence, they develop into fairly similar peak intensity (best seen in the supplementary material), suggesting that they have similar transverse profiles. Hence, we can associate them with the fundamental HE11a and HE11b twin modes, due to their very similar confinement factor and reflectivity,<sup>29,30</sup> rather than the TE01 mode or other high-order twin modes (e.g., HE<sub>21</sub>) which differ in reflectivity.

To confirm this, the threshold material gain of the fundamental HE11 modes is simulated for a variety of NW-diameters around the experimentally measured dimensions and for the photon energies of interest (between 1 eV and 1.15 eV). The resulting data, shown in Fig. 4(c), are further compared to the TE01 mode, which is the mode with overall lowest possible threshold gain. Obviously, our experimental NW-diameter (marked by the dashed line) is found close to the cutoff of the TE01 mode, where the HE11 modes start to dominate, best recognized for lasing energies  $< 1.1 \text{ eV}$ . The minimum threshold gain of the HE11 mode is, however, still by a factor of  $\sim 2\text{--}3$  larger than the lowest possible threshold gain of the TE01 mode, as seen for larger NW-diameters ( $> 400 \text{ nm}$ ). This suggests that the lasing thresholds observed in Fig. 4(b) could be even further reduced by optimizing NW-diameter, while stabilizing the TE01 mode could provide access to unique vector beam lasing profiles as recently observed.<sup>31</sup>

To summarize, we demonstrated lasing from single, ternary GaAsSb NW-lasers at Si-transparent wavelengths ( $\sim 1.1\text{--}1.2 \mu\text{m}$ ) and at temperatures close to room temperature. These advanced, and, in fact, first true ternary near-infrared III-V NW-lasers were enabled by two key factors, i.e., GaAsSb NWs with suitable cavity lengths and the exploitation of lattice-matched InAlGaAs surface passivation with  $> 200$ -fold emission efficiency enhancement. The high-quality NW-lasers were reflected by very low lasing thresholds ( $\sim 3 \mu\text{J}/\text{cm}^2$  at 10 K and  $\sim 45 \mu\text{J}/\text{cm}^2$  at 250 K) that are competitive with the best ever reported III-V NW-lasers in the literature.<sup>1,3,14,16,20,32</sup>

See the supplementary material for EDXS analysis of core-shell NW composition, additional PL spectra and analysis of unpassivated and InAlGaAs-passivated GaAsSb NWs, as well as of NW-laser at 10 K.

The authors sincerely thank H. Riedl for the experimental support, as well as Dr. S. Schmidt and S. Matich for assistance with the preparation of the STEM lamella. This work was supported financially by the ERC project QUANTIC (ID: 771747) funded by the European Research Council. Further support was provided by the Deutsche Forschungsgemeinschaft (DFG) via Project Grant Nos. KO-4005/7-1 and FI-947/4-1 and via Germany's Excellence Strategy-EXC2089/1-390776260 (e-conversion).

## AUTHOR DECLARATIONS

### Conflict of Interest

The authors have no conflicts to disclose.

### Author Contributions

**P. Schmiedeke:** Conceptualization (equal); Data curation (lead); Formal analysis (equal); Investigation (lead); Methodology (equal); Validation (lead); Visualization (equal); Writing – original draft (lead); Writing – review & editing (equal). **C. Doganlar:** Data curation (equal); Formal analysis (equal); Investigation (equal); Methodology (equal); Validation (equal); Visualization (equal); Writing – review &

editing (equal). **H. W. Jeong:** Data curation (supporting); Investigation (supporting); Methodology (supporting); Writing – review & editing (equal). **M. Döblinger:** Data curation (equal); Formal analysis (equal); Investigation (equal); Methodology (equal); Validation (equal); Visualization (equal); Writing – review & editing (equal). **J. J. Finley:** Funding acquisition (equal); Resources (equal). **G. Koblmüller:** Conceptualization (equal); Data curation (equal); Funding acquisition (lead); Investigation (equal); Project administration (lead); Resources (lead); Software (equal); Supervision (lead); Validation (equal); Visualization (equal); Writing – original draft (lead); Writing – review & editing (equal).

## DATA AVAILABILITY

The data that support the findings of this study are available from the corresponding author upon reasonable request.

## REFERENCES

- <sup>1</sup>B. Mayer, L. Janker, B. Loitsch, J. Treu, T. Kostenbader, S. Lichtmannecker, T. Reichert, S. Morkötter, M. Kaniber, G. Abstreiter, C. Gies, G. Koblmüller, and J. J. Finley, *Nano Lett.* **16**, 152 (2016).
- <sup>2</sup>F. Lu, I. Bhattacharya, H. Sun, T.-T. D. Tran, K. W. Ng, G. N. Malheiros-Silveira, and C. Chang-Hasnain, *Optica* **4**, 717 (2017).
- <sup>3</sup>T. Stettner, T. Kostenbader, D. Ruhstorfer, J. Bissinger, H. Riedl, M. Kaniber, G. Koblmüller, and J. J. Finley, *ACS Photonics* **4**, 2537 (2017).
- <sup>4</sup>H. Kim, W.-J. Lee, A. C. Farrell, J. S. D. Morales, P. Senanayake, S. V. Prikhodko, T. J. Ochalski, and D. L. Huffaker, *Nano Lett.* **17**, 5244 (2017).
- <sup>5</sup>M. Takiguchi, A. Yokoo, K. Nozaki, M. D. Birowosuto, K. Tateno, G. Zhang, E. Kuramochi, A. Shinya, and M. Notomi, *APL Photonics* **2**, 046106 (2017).
- <sup>6</sup>M. Takiguchi, N. Takemura, K. Tateno, K. Nozaki, S. Sasaki, S. Sergeant, E. Kuramochi, T. Wasawo, A. Yokoo, A. Shinya, and M. Notomi, *ACS Photonics* **7**, 1016 (2020).
- <sup>7</sup>K. Ren, C. Li, Z. Fang, and F. Feng, *Laser Photonics Rev.* **17**, 2200758 (2023).
- <sup>8</sup>A. Thurn, J. Bissinger, S. Meinecke, P. Schmiedeke, S. S. Oh, W. W. Chow, K. Lüdge, G. Koblmüller, and J. J. Finley, *Phys. Rev. Appl.* **20**, 034045 (2023).
- <sup>9</sup>J. Bissinger, D. Ruhstorfer, T. Stettner, G. Koblmüller, and J. J. Finley, *J. Appl. Phys.* **125**, 243102 (2019).
- <sup>10</sup>W.-Z. Xu, F.-F. Ren, D. Jevtics, A. Hurtado, L. Li, Q. Gao, J. Ye, F. Wang, B. Guilhabert, L. Fu, H. Lu, R. Zhang, H. H. Tan, M. D. Dawson, and C. Jagadish, *Nano Lett.* **18**, 3414 (2018).
- <sup>11</sup>R. Yi, X. Zhang, F. Zhang, L. Gu, Q. Zhang, L. Fang, J. Zhao, L. Fu, H. H. Tan, C. Jagadish, and X. Gan, *Nano Lett.* **22**, 9920 (2022).
- <sup>12</sup>D. Saxena, S. Mokkaapati, P. Parkinson, N. Jiang, Q. Gao, H. H. Tan, and C. Jagadish, *Nat. Photonics* **7**, 963 (2013).
- <sup>13</sup>B. Mayer, D. Rudolph, J. Schnell, S. Morkötter, J. Winnerl, J. Treu, K. Müller, G. Bracher, G. Abstreiter, G. Koblmüller, and J. J. Finley, *Nat. Commun.* **4**, 2931 (2013).
- <sup>14</sup>J. Ho, J. Tatebayashi, S. Sergeant, C. F. Fong, S. Iwamoto, and Y. Arakawa, *ACS Nano* **2**, 165 (2015).
- <sup>15</sup>F. Schuster, J. Kapraun, G. N. Malheiros-Silveira, S. Deshpande, and C. Chang-Hasnain, *Nano Lett.* **17**, 2697 (2017).
- <sup>16</sup>P. Schmiedeke, A. Thurn, S. Matich, M. Döblinger, J. J. Finley, and G. Koblmüller, *Appl. Phys. Lett.* **118**, 221103 (2021).
- <sup>17</sup>G. Zhang, M. Takiguchi, K. Tateno, T. Tawara, M. Notomi, and H. Gotoh, *Sci. Adv.* **5**, eaat8896 (2019).
- <sup>18</sup>T. Stettner, A. Thurn, M. Döblinger, M. O. Hill, J. Bissinger, P. Schmiedeke, S. Matich, T. Kostenbader, D. Ruhstorfer, H. Riedl, M. Kaniber, L. J. Lauhon, J. J. Finley, and G. Koblmüller, *Nano Lett.* **18**, 6292 (2018).
- <sup>19</sup>Y. Tatebayashi, S. Kako, J. Ho, Y. Ota, S. Iwamoto, and Y. Arakawa, *Nat. Photonics* **9**, 501 (2015).
- <sup>20</sup>X. Zhang, R. Yi, N. Gagrani, Z. Li, F. Zhang, X. Gan, X. Yao, X. Yuan, N. Wang, J. Zhao, P. Chen, W. Lu, L. Fu, H. H. Tan, and C. Jagadish, *ACS Nano* **15**, 9126 (2021).
- <sup>21</sup>D. Ren, L. Ahtapodov, J. S. Nilsen, J. Yang, A. Gustafsson, J. Huh, G. J. Conibeer, A. T. van Helvoort, B.-O. Fimland, and H. Weman, *Nano Lett.* **18**, 2304 (2018).
- <sup>22</sup>H. Kim, T.-Y. Chang, W.-J. Lee, and D. L. Huffaker, *Appl. Phys. Lett.* **115**, 213101 (2019).
- <sup>23</sup>M. D. Birowosuto, Y. Yokoo, G. Zhang, K. Tateno, E. Kuramochi, H. Taniyama, M. Takiguchi, and M. Notomi, *Nat. Mater.* **13**, 279 (2014).
- <sup>24</sup>P. Schmiedeke, M. Döblinger, M.-A. Meinhold-Heerlein, C. Doganlar, J. J. Finley, and G. Koblmüller, *Nanotechnology* **35**, 055601 (2023).
- <sup>25</sup>J. Treu, T. Stettner, M. Watzinger, S. Morkötter, M. Döblinger, S. Matich, K. Saller, M. Bichler, G. Abstreiter, J. J. Finley, J. Stangl, and G. Koblmüller, *Nano Lett.* **15**, 3533 (2015).
- <sup>26</sup>F. del Giudice, S. Fust, P. Schmiedeke, J. Pantle, M. Döblinger, A. Ajay, S. Meder, H. Riedl, J. J. Finley, and G. Koblmüller, *Appl. Phys. Lett.* **119**, 193102 (2021).
- <sup>27</sup>J. Treu, M. Bormann, H. Schmeiduch, M. Döblinger, S. Morkötter, S. Matich, P. Wiecha, K. Saller, B. Mayer, M. Bichler, M.-C. Amann, J. J. Finley, G. Abstreiter, and G. Koblmüller, *Nano Lett.* **13**, 6070 (2013).
- <sup>28</sup>L. Balaghi, G. Bussone, R. Grifone, R. Hübner, J. Grenzer, M. Ghorbani-Asl, A. V. Krasheninnikov, H. Schneider, M. Helm, and E. Dimakis, *Nat. Commun.* **10**, 2793 (2019).
- <sup>29</sup>P. Parkinson, J. A. Alanis, K. Peng, D. Saxena, S. Mokkaapati, N. Jiang, L. Fu, H. H. Tan, and C. Jagadish, *Nano Futures* **2**, 035004 (2018).
- <sup>30</sup>D. Saxena, F. Wang, Q. Gao, S. Mokkaapati, H. H. Tan, and C. Jagadish, *Nano Lett.* **15**, 5342 (2015).
- <sup>31</sup>X. Zhang, R. Yi, B. Zheo, C. Li, L. Li, Z. Li, F. Zhang, N. Wang, M. Zhang, L. Fang, J. Zhao, P. Chen, W. Lu, L. Fu, H. H. Tan, C. Jagadish, and X. Gan, *ACS Nano* **17**, 10918 (2023).
- <sup>32</sup>J. A. Alanis, M. Lysevych, T. Burgess, D. Saxena, S. Mokkaapati, S. Skalsky, X. Tang, P. Mitchell, A. S. Walton, H. H. Tan, C. Jagadish, and P. Parkinson, *Nano Lett.* **19**, 362 (2019).